

Appendix A: The good, the bad and the ugly of RbLi

This appendix summarizes the best, the worst and the meh aspects of the RbLi apparatus. Hopefully the items presented can help guide some decisions of future students building experimental apparatuses for ultracold atoms.

A.1 The good

It is very easy to come up with a list of bad things that don't work quite well in the lab. Coming up with a list of good things that work well is harder as we do not tend to think too much about the things that we are not currently fixing. The list below summarizes what I believe are the outstanding good players in the lab.

Overkill transistor banks: Large currents in the lab (quadrupole and Zeeman slower) are controlled with transistor banks formed by a group of MOSFETS whose drain and source are connected in parallel and sharing the same gate voltage that is controlled by a PI servo. The Zeeman slower always operates at a fixed current but the current in the quadrupole coils is dynamically changed throughout the experimental sequence and a fast response is desirable. In 2013 we replaced the quadrupole MOSFET bank with a new unit that contains 20 IXFN 520N075T2 transistors rated for 75 V and 480 A (left panel of Figure 1). Even though our currents

are well below the 480 A limit, the performance of the transistors really decays as the drain to source voltage is increased as can be seen in the right panel of Figure 1. The use of more transistors reduces the power dissipation of each individual transistor which allows us to operate the power supply at a higher voltage of 15 V that helps counteract the inductive kickback of the coils. With the new transistor bank the turn on time of the coils was reduced from 100 ms to 5 ms leading to improved magnetic trapping and better Stern-Gerlach pulses for imaging, only with an unavoidable small number of blown off transistors.

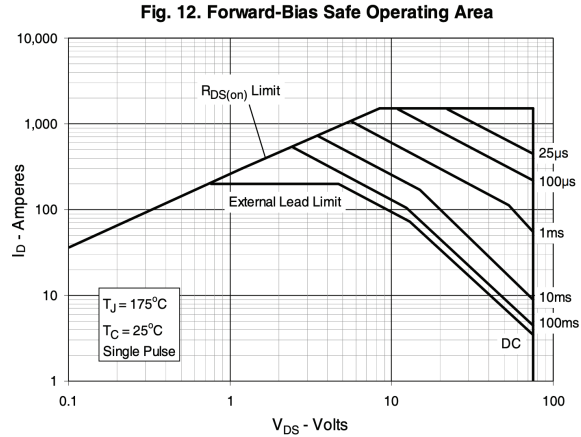
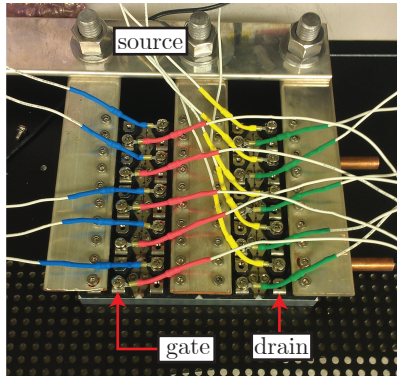


Figure 1: Left: New MOSFET bank. Right: Safe operation regime of the IXFN 520N075T2 MOSFET. Even though they are in principle rated for up to 480 A the maximum safe current is greatly reduced at larger drain to source voltages V_{DS} . A high V_{DS} is desirable to reduce the inductive kickback during turn on.

Oven chamber including hand made in vacuum shutters: Before going into the Zeeman slower, the atoms that are heated in the Rb oven travel to the main oven chamber that is pictured in Figure 2b containing a cold-cup and an oven shutter. The cold-cup is a cylindrical shaped copper piece that is attached to the cold end of a thermo-electric cooler (TEC) via a copper rod. We keep the cold-

cup temperature at -30 C in order to capture excess Rb atoms in the chamber and prevent damaging the ion pumps. The oven shutter allows us to block after the MOT loading stage to prevent unwanted heating. We use a homemade device, made from a re-purposed hard drive disk shutter with a metallic flag attached to its end. The shutter is electrically connected to an electric feedthrough with vacuum-compatible Kapton sealed wires. Other apparatus within the JQI [146] have commercial shutters from **Uniblitz** and some of them have failed in the past. Overall we have found this setup to be very reliable. The only problem we experienced once was some accumulation of Rb on the cold cup that started blocking the atomic beam. To remedy this we reversed the polarity of the TEC and heated the cold cup barely enough so that the accumulated Rb atoms melted and moved away from the aperture of the atomic beam.

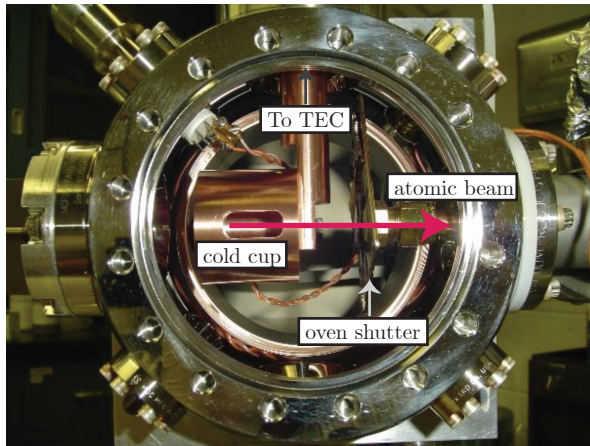


Figure 2: The RbLi oven chamber. We use a cold cup to prevent excess Rb atoms from damaging the ion pumps and a homemade in-vacuum shutter to block the atomic beam after the MOT stage to prevent heating of the atoms at later stages.

Ultraviolet LEDs: We have two 3 W ultraviolet LEDs from **Mightex** placed at the glass cell side of the vacuum system. One is aimed at the vacuum window

where the slower beam enters and the other is placed aiming at the glass cell. The LEDs prevent Rubidium from depositing on the vacuum system and can conveniently be turned on and off with a TTL signal from the computer. We have found that routinely turning them on (for example, leaving them on overnight) leads to a smoother operation of the system.

Mirror mounts with picomotor actuators: We use 8816-6 picomotor optical mounts from **New Focus Optics** whose deflection angle can be electronically adjusted on the order of microradians. The addition of picomotor mounts has made alignment of laser beams to the atoms significantly easier. We use this mounts on the last tunable mirror before the atoms for beam paths whose alignment is critical, for example in optical dipole trap and Raman beams.

Polarizers on MOT beams: This item is a bad thing disguised as a good thing. The light of our MOT beams is coupled to polarization maintaining optical fibers. We found that despite our best efforts to align the polarization of the incoming light to the slow/fast axis of the fiber the fluctuations in the output polarization could cause considerable instabilities in the BEC production. To keep the polarization clean we placed polarizers at the output of the fibers. We found that despite the power hit we get from the changes in polarization, this solution leads to a much more stable production of BECs.

Lab couch: When the experiment is functional enough that data can be taken long hours in the lab are often required. If it gets late, the lab couch allows the person running the experiment to take small naps as the data keeps coming while still being close to the apparatus in case something needs to be fixed. A slightly

rested grad student tends to take less poor decisions than an exhausted grad student.

Other elements already mentioned in the main text: The new master laser from Vescent photonics has been very stable and reliable. The new Mako camera has been very helpful to get rid of unwanted fringes in absorption images. Labscript makes writing experimental sequences very straightforward.

A.2 The bad

The bad, these are elements of the apparatus that were constant sources of pain and if considering a new experimental design should be avoided.

Water cooling shared between two labs: The quadrupole and Zeeman slower coils as well as the transistor banks require water cooling due to Joule heating. Our lab space is shared with a Rubidium-Ytterbium ultracold mixtures apparatus [147] and amongst the things we share is the water cooling system. The schematic in Figure 3 illustrates a simplified layout of the water cooling system. The water was filtered at two different points, first each line has a $440\text{ }\mu\text{m}$ particulate filter from Swagelok and then the water returning to the heat exchanger is filtered with a low-impedance cellulose cartridge (McMaster 7191K11). Both filters only capture impurities in the water for one given flow direction. One of the failure modes which occurs when one of the booster pumps is turned on before the heat exchanger, causing water to flow from one experiment to the other and bringing a collection of nasty things that escapes the filters into the coils. Over the years our system has suffered of clogged filters, clogged coils and broken booster pumps. For

best operation it is highly recommended that the cartridge filter is changed and that the Swagelok filters be cleanded at least once a year and that a 10% solution of an anti-corrosive Optishield Plus in water is used as a coolant. Even when following this practices, we managed to find lots of gunk and unidentified objects (sand? glass? mud? oxide? dead bacteria?) in the water, just at a slower rate. Besides this issue, just having to interrupt the operation of two experiments whenever any plumbing works needs to be done on one experiment is quite inconvenient.

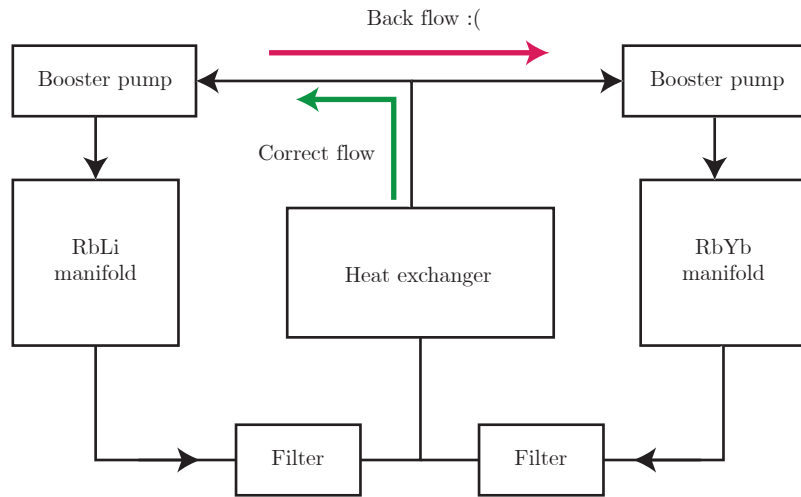


Figure 3: Simplified schematic of the shared water cooling manifold.

Flipper mirrors: The optical path of the MOT beams near the atoms is very close to that of Raman, optical dipole trap and probe beams. Since the MOT beams are only used at the early stages of the experiment it is tempting to use flipper mirror mounts so that once they are no longer needed they can be moved away to make space for other beams. This was the approach originally taken in the lab and we used 8893-K motorized optical flipper mounts from Newport in multiple

locations. As they break over and over again, they have been slowly replaced by more stable solutions such as periscopes or polarizing beam splitters wherever it is possible. Flipper mirrors are always bound to break, it is only a matter of time before it happens. Avoid using them unless you absolutely have no alternative.

Optical fibers right below air vents: The optical fibers connecting the main experiment optical table and the laser optical table are routed close to a pair of AC vents in the lab. The changes in air temperature result in polarization fluctuations at the output of optical fibers (see previous section about MOT polarizers), a constant cause of pain and instability in our BEC production. We have tried to remedy this issue by partially blocking vents and enclosing the fibers in a large PVC tube.

Free spaced dipole laser: The laser system providing 1064 nm light for the optical dipole trap is not fiber coupled and is setup in the same optical table as the vacuum system; we are not able to change the laser without destroying the alignment of the dipole trap with the atoms. This issue became relevant while setting up a 1D optical lattice by retro-reflecting one of the dipole trap beams as we noticed that the laser mode changes on a very fast timescale, leading to large fluctuations in the optical lattice. In the original design of the laser the light was meant to be fiber coupled using high-power photonic crystal fibers but they did not have built in mode expanders which resulted in the tip of the fibers repeatedly getting burnt after some time of use. In short, mode expanders are recommended in applications involving large optical powers.

A.3 The ugly

The ugly elements are not quite bad but they don't function flawlessly either.

If given the option to replace them with something better I definitely would.

Kepco bipolar power supplies: We use three Kepco BOP 20-20M bipolar power supplies to provide the current for the bias coils. While it is nice to have a commercially available power supply that can provide $\pm 20\text{ A}$ they come with a few drawbacks. First the current they provide has 60 Hz noise in it and in order to suppress it and stabilize the currents we must use a PI feedback circuit. The power supplies has multiple banks of NPN and PNP transistors inside mounted on a big heat sink with fans attached to it making them quite noisy; it is not optimal to place them close to the main experiment chamber and long connections open the door to unwanted ground loops. Additionally they have a few failure modes. All the problems we experienced whenever they stopped working (e.g. the output current railing) were symptoms of malfunctioning transistors, something that we experienced on multiple occasions.

Toptica's BoosTA: Our cooling light comes from a Toptica DL Pro laser that is amplified using a Toptica BoosTA tapered amplifier system. The output power of this TA has been relatively stable over the years, in fact it has been operating for over 7 years now without the need of replacing the TA chip, unlike a homemade TA setup (see [36, 37]). The downside is it has a tendency to turn itself off and on its worst days it would turn off so often that it would be impossible to operate the experiment. We have not been able to identify the problem despite our

best efforts to look into the TA controller, the TA itself, multiple conversations with Toptica engineers, etc.

Too many USB devices connected to the same computer: We use multiple USB-6229 data acquisition (DAQ) devices from **National Instruments**. They are located at different points of the lab and then connected to the control computer through USB to optical fiber adapters that break the ground between the computer and the rest of the lab equipment (a practice we always try to follow when connecting things to the computer). We have a total of 6 NI devices in addition to other equipment like oscilloscopes all connected to the computer through BNC cables. Often times we struggled with the computer failing to detect one or multiple devices and it would take a very special (and different every time) combination of plugging and unplugging, turning off and turning back on things until all devices were recognized by the computer. We observe that the problem occurs less often when we don't have as many USB devices connected to the computer.

Appendix B: New apparatus

As mentioned in the main text, the construction of a new apparatus for producing BECs of ^{87}Rb and ^{39}K is underway. The design of the apparatus is intended to be a bug fix version of the RbChip [148] lab at NIST. The new apparatus does not have a Zeeman slower and instead will use magnetic transport coils to move atoms from a MOT cell to the main science cell.

This Appendix describes some aspects of the design and construction of the new apparatus where I was involved. Disclaimer: none of this things have been tested yet so we don't know yet if it will all work horribly. I have tried to include an extensive list of the part numbers used so they can be used as a future reference.

B.1 Water cooling

The lack of a Zeeman slower in the apparatus greatly simplifies the water cooling system compared to that of RbLi. Since we don't anticipate to have any coils with high flow impedance we expect that the pressure from a recirculating chiller will be enough to provide water cooling to the transistor banks and the magnetic transport coils.

Our choice of chiller was the TF1LN400-LN 1.4 kW recirculating chiller from

Thermo Fisher Scientific. The water is filtered both at the output and the return with a high-impedance filter with a cellulose cartridge filter(replacement filter: McMaster 4422K3, filter housing: McMater 7191K11). A breakout manifold divides the chilled water into 5 different lines, each one with a flow meter (Proteus Industries 0101C110) that can be used to interlock the current of water cooled applications to the flow of water. Based on previous experiences with plumbing (see Appendix A) I highly encourage replacing the filters at least once a year and to use a solution of 10% corrosion inhibitor (e.g. OptiShield Plus) and distilled water as a coolant.

a. Service corridor side



b. Experiment side

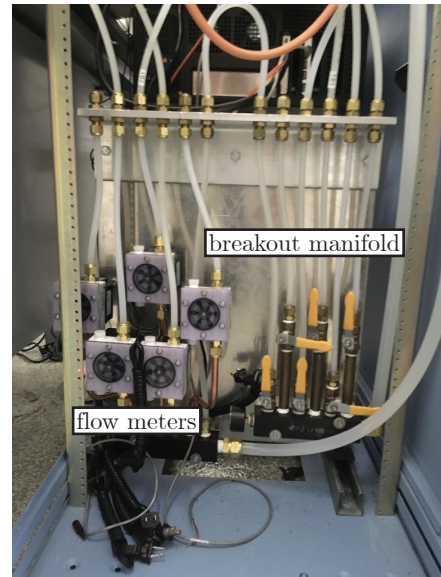


Figure 1: Water cooling

B.2 Electrical installation

We have two Agilent 6690A (440 A at 15 V max. current) to provide all the necessary currents. The power supplies are located in the service corridor and are connected to three copper bars corresponding to ± 15 V and ground using welding cable (McMaster 7818A17) that is laid on cable trays (McMaster 30065T11 and similar). The copper bars serve as a hub for power distribution inside the lab where lab devices such as transistor banks can be connected. The positive and negative terminals of the power supplies have two cables attached to them and they are all arranged in the pattern shown in Figure 2 so that the magnetic field produced by currents in them is closer to a magnetic quadrupole which decays faster than the field of a magnetic dipole. We are trying to minimize unwanted magnetic fields at the experiment and being nice to our neighbors as well. We are not planning to use commercial bipolar power supplies in this lab (see Appendix A) and instead we will be using a MOSFET based homemade supply that will draw current from the ± 15 V rails.

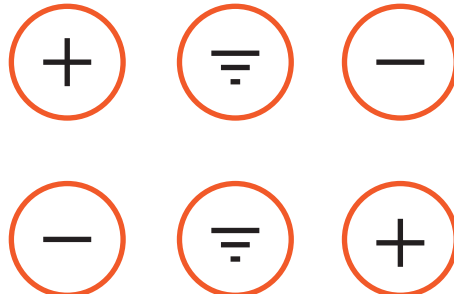


Figure 2: Configuration of the welding cables connecting the power supplies to equipment in the lab.



Figure 3: A roller coaster ride, from the power supplies in the service corridor to three copper bars that distribute the power.

B.3 Coil winding

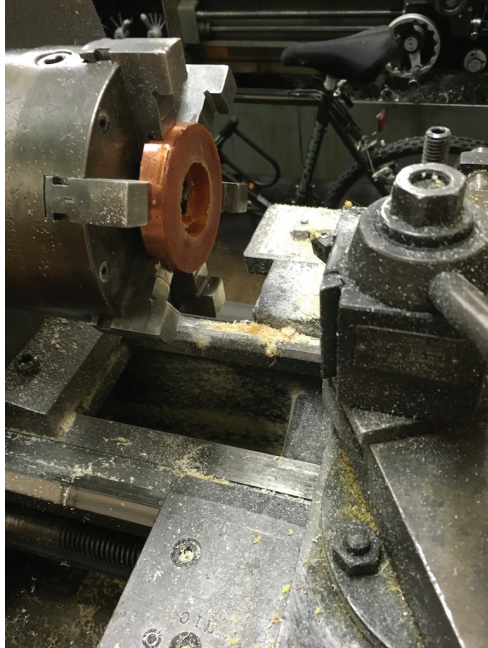
All the coils in the apparatus including magnetic transport, bias and gradient cancellation will be made of ribbon wire (**Laminax** from **Bridgeport Magnetics**). We followed the coil fabrication process described in [148] which involves first winding a fixed number of turns around a prefabricated form with a particular geometry. The coils were then covered with a machinable epoxy (**Stycast 1266**) to fill in any air gaps. A lesson we learned while doing this is that only room temperature epoxy should be mixed. We keep the epoxy in a fridge to extend its lifetime but if it is cold some tiny drops of water will condense in it as it is being mixed and it will not properly be cured. To minimize the air bubbles inside the epoxy we placed the coils on a vacuum bell and we pumped the air out using an electric vacuum pump (**McMaster 4396K21**). After the epoxy has cured (overnight if it is left at room temperature or less if it is left at higher temperature) the coils

are ready for lathing to remove all excess epoxy and kapton tape up to the surface of the copper. After some trial and error (and lots of frustration) we found that using a diamond tip cutter (McMaster 3316A32) and spinning the lathe not faster than 150 rpm gives the best results. Using a cutter that is not sharp enough or cutting too aggressively close to the soft copper results in deformed traces that merge into each other causing unwanted shorts. The coils of the RbChip apparatus were machined at NIST using a special aluminum form to mount the coils on the lathe (see. The machinist at UMD considered this was not safe enough so I instead had to mount the coils using a 6 jaw chuck as shown in Figure 4a. For anyone making coils in the future: it is sort of an art to get it right and screwing up many coils at the beginning is part of learning the art. That being said, an important aspect of learning the ‘art’ right be as careful and consistent as possible from the start.

B.4 Rb source and ‘oven’

The new apparatus will have a cold ‘oven’ to keep the vapor pressure low connected to a glass cell where light induced atomic desorption (LIAD) [149] will be used to increase the Rb vapor pressure for MOT loading using non-thermal means. The Rb source consists of a 1.33” CF flanged bellow (Kurt J. Lesker MH-CF-A03) with a Rb ampule. The bellow is housed in the ‘oven’ which is designed to keep the source at temperatures near 1 C. The oven is made of hollow aluminum cylinder with a slit on one side with tapped holes so that 1/4 – 20 screws can be used to tighten it and fix the oven to the source. The bottom of the oven attaches to the

a. Coil mounted on lathe



b. Coils before and after lathing



c. Coil labeling system



Figure 4: **a.** I used a six jaw chuck and a diamond cutter on the lathe to remove the excess epoxy and kapton on the coils. **b.** Coils before (left) and after lathing (right). **c.** A good labeling system is important to keep to ensure uniformity of coils. The ‘Wartortle’ coil shown here has 64 turns. During fabrication we keep track of all the number of turns and resistance of all coils in a table.

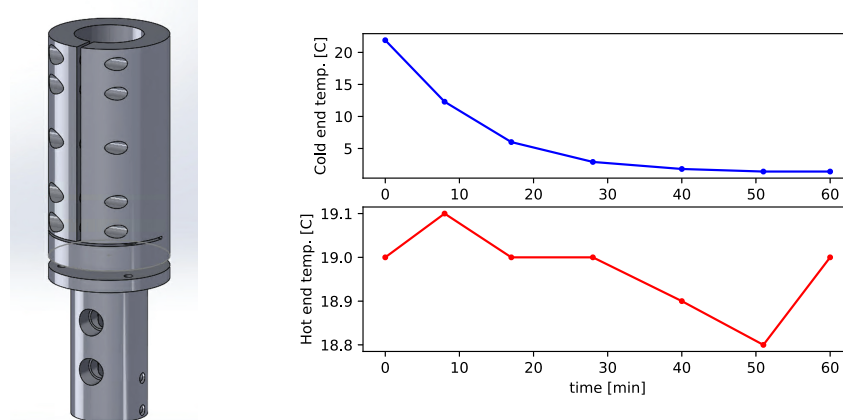
cold end of a TEC that provides the cooling. The hot side of the TEC is attached to a heat sink made of a hollow brass piece with tapped holes for 1/4" NPT pipes that will be used to provide water cooling. Figure 5a shows CAD drawings of both of this parts.

We tested the performance of a prototype without any vacuum systems attached to it. We applied a 2 A current to two TECs (Digikey 102-1664-ND) sandwiched in between the heat sink and oven. The heat sink was water cooled using $\approx [18]C$ water. Figure 5b shows the temperature of both the oven side (top) and the heat sink side (bottom) of the assembly. We did not use any insulation for this

test to prevent condensation (see Figure 5c right) which should be done once its installed on the apparatus.

Our initial plan was to control the temperature using a linear temperature controller designed at the JQI (the design is available at the [JQI GitHub](#)) interfaced to the lab computer and Labscript using a serial to ethernet adapter ([WIZnet WIZ107SR](#)). This project is not completed to this date.

a. Rb ‘oven’ and heat sink b. Bench test temperatures



c. Testing prototype oven and heat sink

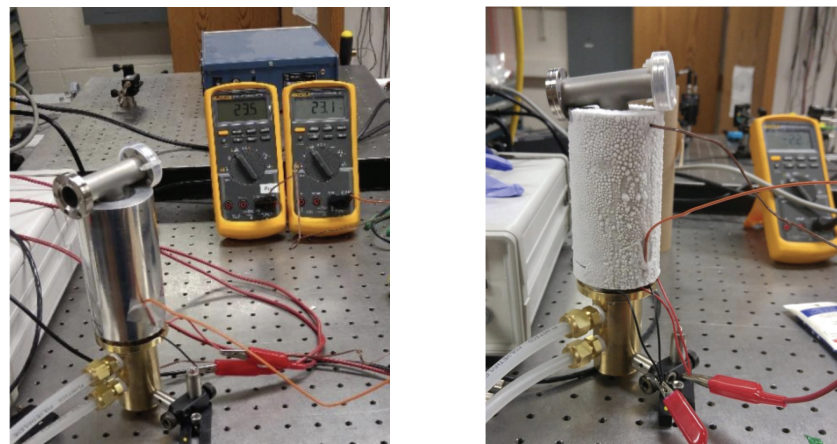


Figure 5: Rubidium oven assembly

B.5 Table enclosures

The enclosures of the optical tables are made of **Alumalite** from **Laminators Inc.** mounted on frames made out of aluminum extrusions from 80/20 and sliding tracks (2220 and 2210). Alumalite is a sandwich of a corrugated corrugated polypropylene material in between two thin sheets of aluminum. We chose this material because it is strong and lightweight. Its laser safety properties remain to be tested but we anticipate it is better than the acrylic panels at the RbLi lab which are essentially transparent at 1064 nm.

To the new and future members of the lab: I sincerely hope the things I designed and built don't cause you much pain!

Appendix C: Full derivation of the Raman coupled $|xyz\rangle$ states

In this Appendix I derive the full time-dependent Hamiltonian describing the $|xyz\rangle$ states coupled by three Raman beams to produce Rashba type SOC (see Chapter 8). It takes a bit of thinking to understand what the frequencies of the different Raman coupling terms correspond to in the RF rotating frame where the $|xyz\rangle$ states are defined. Hopefully this Appendix helps to clarify our specific choices for the laser geometry and polarization.

Our system is based on the proposal described in [22] to engineer a system with Rashba-like SOC. We consider ^{87}Rb atoms in the ground hyperfine $F = 1$ manifold subject to a constant magnetic field $B_0\mathbf{e}_z$ and an RF magnetic field $B_{\text{RF}} \cos(\omega_{\text{RF}}t)\mathbf{e}_x$ as in Chapter 6. The system is described by the Hamiltonian

$$\hat{H}_{\text{RF}} = \omega_0 \hat{F}_z - \frac{\epsilon}{\hbar} (\hat{F}_z^2 - \mathbb{1}) + 2\Omega_{\text{RF}} \cos(\omega_{\text{RF}}t) \hat{F}_x, \quad (\text{C.1})$$

where $\omega_0 = g_F \mu_B B_0$ is the Larmor frequency, ϵ is a quadratic Zeeman shift that breaks the degeneracy of the $|m_F = -1\rangle \leftrightarrow |m_F = 0\rangle$ and $|m_F = 1\rangle \leftrightarrow |m_F = 0\rangle$ transitions, $\Omega_{\text{RF}} = g_F \mu_B B_{\text{RF}}/2$ is the RF coupling strength and $\mathbb{1}$ is the identity matrix. We transform the Hamiltonian into the RF rotating frame using the unitary transformation $\hat{U}(t) = \exp(-i\omega_{\text{RF}}t \hat{F}_z)$. The spin-1 operators under this transforma-

tion become

$$\begin{aligned}
\hat{F}_x &\rightarrow \cos(\omega_{\text{RF}}t)\hat{F}_x - \sin(\omega_{\text{RF}}t)\hat{F}_y \\
&= e^{i\omega_{\text{RF}}t}\hat{F}_+ + e^{-i\omega_{\text{RF}}t}\hat{F}_- \\
\hat{F}_y &\rightarrow \sin(\omega_{\text{RF}}t)\hat{F}_x + \cos(\omega_{\text{RF}}t)\hat{F}_y \\
&= \frac{1}{i}(e^{i\omega_{\text{RF}}t}\hat{F}_+ - e^{-i\omega_{\text{RF}}t}\hat{F}_-) \\
\hat{F}_z &\rightarrow \hat{F}_z.
\end{aligned} \tag{C.2}$$

The unitary evolution in the rotating frame is described by the transformed Hamiltonian $\hat{U}^\dagger(t)(\hat{H}_{\text{RF}} - i\hbar\partial_t)\hat{U}(t)$, which after neglecting terms that are oscillating with angular frequency $2\omega_{\text{RF}}$ is

$$\hat{H}_{\text{RWA}} = \Delta\hat{F}_z - \frac{\epsilon}{\hbar}(\hat{F}_z^2 - \mathbb{I}) + \Omega_{\text{RF}}\hat{F}_x \tag{C.3}$$

The eigenstate of Equation C.3 are the $|xyz\rangle$ states described in Chapter 6. Now

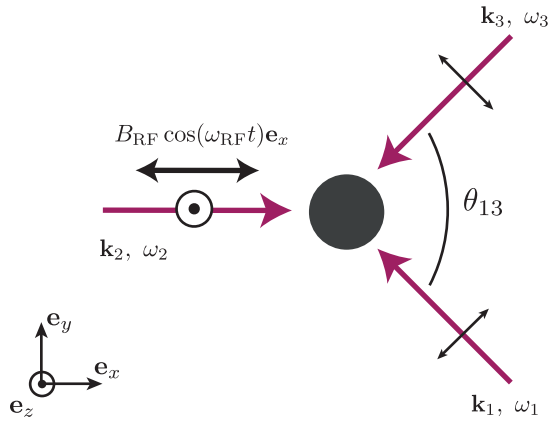


Figure 1: Laser layout: We use a strong RF field and three linearly polarized Raman beams propagating in the xy plane couple the $|xyz\rangle$ states and engineer the Rashba Hamiltonian.

we apply three Raman beams as shown in Figure 1. This configuration differs from the one proposed in [22] for technical reasons as we wanted all the Raman recoil vectors to lie within the imaging plane of the experiment which corresponds to the xy plane.

The electric field at the atoms in the lab (not rotating) frame is

$$\mathbf{E}(x, t) = \sum_{i=1}^3 E_i \mathbf{e}_i e^{i(\mathbf{k}_i \cdot \mathbf{x} - \omega_i t)}, \quad (\text{C.4})$$

where E_i is the field amplitude, ω_i is the angular frequency, \mathbf{k}_i is the wave vector and \mathbf{e}_i is the polarization of each of the beams. In order to have the right coupling matrix elements to cyclically couple all three states in a ring-like coupling as described in [132] we need a Hamiltonian of the form

$$\hat{H}_{\text{SOC}} = (\Omega_x, \Omega_y, \Omega_z) \cdot \hat{\mathbf{F}} \quad (\text{C.5})$$

(see Section 6.3.3). This is possible if we choose two Raman beams to have in plane polarization and one vertically polarized beam:

$$\begin{aligned} \mathbf{e}_1 &= \frac{(k_{1y}, -k_{1x}, 0)}{||\mathbf{k}_1||^2}, \\ \mathbf{e}_2 &= (0, 0, 1), \\ \mathbf{e}_3 &= \frac{(k_{3y}, -k_{3x}, 0)}{||\mathbf{k}_3||^2}, \end{aligned} \quad (\text{C.6})$$

The Raman coupling strength is proportional to the vector polarizability (see

Section 3.3.2) and the Hamiltonian describing the atom-light coupling is

$$\hat{H}_R = (iu_v \mathbf{E} \times \mathbf{E}^*) \cdot \hat{\mathbf{F}}, \quad (\text{C.7})$$

where u_v is the vector polarizability. The expression for the cross product of the electric field at the atoms is quite messy, lets rewrite it in a more convenient way:

$$\begin{aligned} \mathbf{E} \times \mathbf{E}^* &= (E_1^* \mathbf{e}_1 e^{-i(\mathbf{k}_1 \cdot \mathbf{x} - \omega_1 t)} + E_2^* \mathbf{e}_2 e^{-i(\mathbf{k}_2 \cdot \mathbf{x} - \omega_2 t)} + E_3^* \mathbf{e}_3 e^{-i(\mathbf{k}_3 \cdot \mathbf{x} - \omega_3 t)}) \times c.c \\ &= E_1^* E_2 (\mathbf{e}_1 \times \mathbf{e}_2) e^{i[(\mathbf{k}_2 - \mathbf{k}_1) \cdot \mathbf{x} - (\omega_2 - \omega_1)t]} + E_1^* E_3 (\mathbf{e}_1 \times \mathbf{e}_3) e^{i[(\mathbf{k}_3 - \mathbf{k}_1) \cdot \mathbf{x} - (\omega_3 - \omega_1)t]} \\ &\quad + E_2^* E_1 (\mathbf{e}_2 \times \mathbf{e}_1) e^{i[(\mathbf{k}_1 - \mathbf{k}_2) \cdot \mathbf{x} - (\omega_1 - \omega_2)t]} + E_2^* E_3 (\mathbf{e}_2 \times \mathbf{e}_3) e^{i[(\mathbf{k}_3 - \mathbf{k}_2) \cdot \mathbf{x} - (\omega_3 - \omega_2)t]} \\ &\quad + E_3^* E_1 (\mathbf{e}_3 \times \mathbf{e}_1) e^{i[(\mathbf{k}_1 - \mathbf{k}_3) \cdot \mathbf{x} - (\omega_1 - \omega_3)t]} + E_3^* E_2 (\mathbf{e}_3 \times \mathbf{e}_2) e^{i[(\mathbf{k}_2 - \mathbf{k}_3) \cdot \mathbf{x} - (\omega_2 - \omega_3)t]} \\ &= 2i \left[(\mathbf{e}_1 \times \mathbf{e}_2) \text{Im}\{E_1^* E_2 e^{i(\mathbf{k}_{21} \cdot \mathbf{x} - \omega_{21}t)}\} \right. \\ &\quad + (\mathbf{e}_1 \times \mathbf{e}_3) \text{Im}\{E_1^* E_3 e^{i(\mathbf{k}_{32} \cdot \mathbf{x} - \omega_{32}t)}\} \\ &\quad \left. + (\mathbf{e}_2 \times \mathbf{e}_3) \text{Im}\{E_2^* E_3 e^{i(\mathbf{k}_{32} \cdot \mathbf{x} - \omega_{32}t)}\} \right] \end{aligned} \quad (\text{C.8})$$

and using the definition of the polarization vectors (Equation C.6)

$$\begin{aligned} \mathbf{e}_1 \times \mathbf{e}_2 &= \frac{(-k_{1x}, -k_{1y}, 0)}{||\mathbf{k}_1||^2} = -\hat{\mathbf{k}}_1 \\ \mathbf{e}_1 \times \mathbf{e}_3 &= \frac{(0, 0, -k_{1y}k_{3x} + k_{3y}k_{1x})}{||\mathbf{k}_1||^2 ||\mathbf{k}_3||^2} = \mathbf{e}_z \sin \theta_{13} \\ \mathbf{e}_2 \times \mathbf{e}_3 &= \frac{(k_{3x}, k_{3y}, 0)}{||\mathbf{k}_3||^2} = \hat{\mathbf{k}}_3, \end{aligned} \quad (\text{C.9})$$

we obtain the the desired Hamiltonian describing the atom light interaction

$$\begin{aligned} iu_v \mathbf{E}^* \times \mathbf{E} \cdot \hat{\mathbf{F}} &= -2u_v \left[-\hat{\mathbf{k}}_1 \text{Im}\{12\} + \mathbf{e}_z \sin \theta_{13} \text{Im}\{13\} + \hat{\mathbf{k}}_3 \text{Im}\{23\} \right] \cdot \hat{\mathbf{F}} \\ &= (\Omega_x, \Omega_y, \Omega_z) \cdot \hat{\mathbf{F}}, \end{aligned} \quad (\text{C.10})$$

where

$$\begin{aligned} \Omega_x &= \frac{k_{1x}}{\|\mathbf{k}_1\|} \text{Im}\{\Omega_{12} e^{i(\mathbf{k}_{21} \cdot \mathbf{x} - \omega_{21} t)}\} + \frac{k_{3x}}{\|\mathbf{k}_3\|} \text{Im}\{\Omega_{23} e^{i(\mathbf{k}_{32} \cdot \mathbf{x} - \omega_{32} t)}\} \\ \Omega_y &= \frac{k_{1y}}{\|\mathbf{k}_1\|} \text{Im}\{\Omega_{12} e^{i(\mathbf{k}_{21} \cdot \mathbf{x} - \omega_{21} t)}\} + \frac{k_{3y}}{\|\mathbf{k}_3\|} \text{Im}\{\Omega_{23} e^{i(\mathbf{k}_{32} \cdot \mathbf{x} - \omega_{32} t)}\} \\ \Omega_z &= \text{Im}\{\Omega_{13} e^{i(\mathbf{k}_{31} \cdot \mathbf{x} - \omega_{31} t)}\}, \end{aligned} \quad (\text{C.11})$$

and

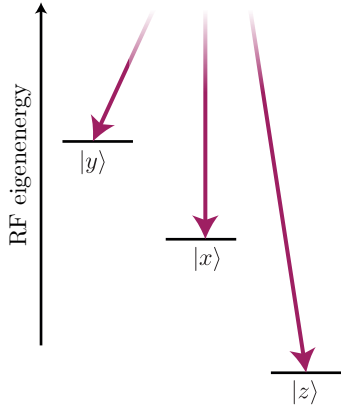
$$\begin{aligned} \Omega_{12} &= 2u_v E_1^* E_2 \\ \Omega_{13} &= -2u_v E_1^* E_3 \sin \theta_{13} \\ \Omega_{23} &= -2u_v E_2^* E_3. \end{aligned} \quad (\text{C.12})$$

Now we need to transform Eq. C.10 into the rotating frame, this is where things start getting fun. The ‘slow’ or ‘fast’ nature of a given term depends on the specific choice of frequencies on each Raman beam which should be such that the frequency differences ω_{ij} are resonant with dressed state transitions in the rotating frame as shown in Figure 2a.

I showed in Equation C.2 that in the rotating frame the \hat{F}_x and \hat{F}_y operators get additional factors of $\exp(\pm i\omega_{\text{RF}})$ while \hat{F}_z remains unchanged. We must therefore have the frequencies of beams giving rise to \hat{F}_x and \hat{F}_y coupling to differ in

frequency by an additional ω_{RF} and the beams that give the \hat{F}_z coupling to be close in frequency. The two possible ways of doing so are shown in Figure 2b and they determine whether ω_{21} and ω_{31} are positive or negative.

a. Resonant Raman coupling



b. Possible Raman laser frequency configurations

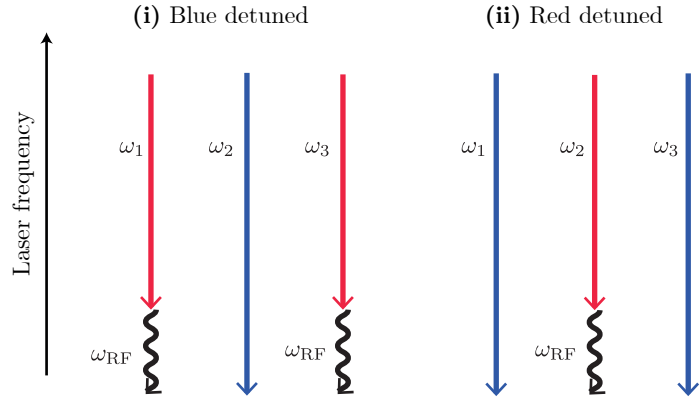


Figure 2: **a** The choice of laser frequencies should be such that in the frame rotating with frequency ω_{RF} we get resonant Raman coupling of the $|xyz\rangle$ states. **b.** Possible laser frequency configurations: **i)** Blue detuned configuration: There are 2 frequencies smaller by about ω_{RF} and one larger frequency. **ii)** The red detuned configuration: there are 2 frequencies that are larger by about ω_{RF} and one smaller frequency.

Lets look at the firs term of the $\Omega_x \hat{F}_x$ coupling to get an idea of how the RWA

will work here:

$$\begin{aligned}
\Omega_x^{(1)} \hat{F}_x &\rightarrow \frac{1}{4i} \frac{k_{1x}}{\|\mathbf{k}_1\|} \left(\Omega_{12} e^{i(\mathbf{k}_{21} \cdot \mathbf{x} - \omega_{21})t} - \Omega_{12}^* e^{-i(\mathbf{k}_{21} \cdot \mathbf{x} - \omega_{21}t)} \right) \left(e^{i\omega_{\text{RF}}t} \hat{F}_+ + e^{-i\omega_{\text{RF}}t} \hat{F}_- \right) \\
&\approx \frac{1}{4i} \frac{k_{1x}}{\|\mathbf{k}_1\|} \left(\Omega_{12} e^{i(\mathbf{k}_{21} \cdot \mathbf{x} - (\omega_{21} \mp \omega_{\text{RF}})t)} \hat{F}_\pm - \Omega_{12}^* e^{-i(\mathbf{k}_{21} \cdot \mathbf{x} - (\omega_{21} \mp \omega_{\text{RF}})t)} \hat{F}_\mp \right) \\
&= \frac{1}{2} \frac{k_{1x}}{\|\mathbf{k}_1\|} |\Omega_{12}| \left(\sin[\mathbf{k}_{21} \cdot \mathbf{x} - (\omega_{21} \mp \omega_{\text{RF}})t + \phi_{12}] \hat{F}_x \right. \\
&\quad \left. \pm \cos[\mathbf{k}_{21} \cdot \mathbf{x} - (\omega_{21} \mp \omega_{\text{RF}})t + \phi_{12}] \hat{F}_y \right).
\end{aligned} \tag{C.13}$$

Here the upper sign corresponds to the $\omega_{21} > 0$ case (blue detuned) and the lower sign to $\omega_{21} < 0$ (red detuned) and I performed a RWA approximation in the second line by neglecting the terms oscillating with frequency close to $2\omega_{\text{RF}}$. Similarly, the second term of $\Omega_x \hat{F}_x$ is

$$\begin{aligned}
\Omega_x^{(2)} \hat{F}_x &\rightarrow \frac{1}{4i} \frac{k_{3x}}{\|\mathbf{k}_3\|} \left(\Omega_{23} e^{i(\mathbf{k}_{32} \cdot \mathbf{x} - \omega_{32})t} - \Omega_{23}^* e^{-i(\mathbf{k}_{32} \cdot \mathbf{x} - \omega_{32}t)} \right) \left(e^{i\omega_{\text{RF}}t} \hat{F}_+ + e^{-i\omega_{\text{RF}}t} \hat{F}_- \right) \\
&\approx \frac{1}{2} \frac{k_{3x}}{\|\mathbf{k}_3\|} |\Omega_{23}| \left(\sin[\mathbf{k}_{32} \cdot \mathbf{x} - (\omega_{32} \mp \omega_{\text{RF}})t + \phi_{23}] \hat{F}_x \right. \\
&\quad \left. \pm \cos[\mathbf{k}_{32} \cdot \mathbf{x} - (\omega_{32} \mp \omega_{\text{RF}})t + \phi_{23}] \hat{F}_y \right)
\end{aligned} \tag{C.14}$$

where I used the same sign convention as before. It is important to keep in mind that if ω_{21} is positive then ω_{32} must be negative and vice versa. Lets keep cranking

the algebra!

$$\begin{aligned}
\Omega_y^{(1)} \hat{F}_y &\rightarrow -\frac{1}{4} \frac{k_{1y}}{\|\mathbf{k}_1\|} \left(\Omega_{12} e^{i(\mathbf{k}_{21} \cdot \mathbf{x} - \omega_{21} t)} - \Omega_{12}^* e^{-i(\mathbf{k}_{21} \cdot \mathbf{x} - \omega_{21} t)} \right) \left(e^{i\omega_{\text{RF}} t} \hat{F}_+ - e^{-i\omega_{\text{RF}} t} \hat{F}_- \right) \\
&\approx \mp \frac{1}{4} \frac{k_{1y}}{\|\mathbf{k}_1\|} \left(\Omega_{12} e^{i(\mathbf{k}_{21} \cdot \mathbf{x} - (\omega_{21} \mp \omega_{\text{RF}})t)} \hat{F}_\pm + \Omega_{12}^* e^{-i(\mathbf{k}_{21} \cdot \mathbf{x} - (\omega_{21} \mp \omega_{\text{RF}})t)} \hat{F}_\mp \right) \\
&= \mp \frac{1}{2} \frac{k_{1y}}{\|\mathbf{k}_1\|} |\Omega_{12}| \left(\cos[\mathbf{k}_{21} \cdot \mathbf{x} - (\omega_{21} \mp \omega_{\text{RF}})t + \phi_{12}] \hat{F}_x \right. \\
&\quad \left. - \sin[\mathbf{k}_{21} \cdot \mathbf{x} - (\omega_{21} \mp \omega_{\text{RF}})t + \phi_{12}] \hat{F}_y \right), \\
\end{aligned} \tag{C.15}$$

$$\begin{aligned}
\Omega_y^{(2)} \hat{F}_y &\rightarrow -\frac{1}{4} \frac{k_{3y}}{\|\mathbf{k}_3\|} \left(\Omega_{23} e^{i(\mathbf{k}_{32} \cdot \mathbf{x} - \omega_{32} t)} - \Omega_{23}^* e^{-i(\mathbf{k}_{32} \cdot \mathbf{x} - \omega_{32} t)} \right) \left(e^{i\omega_{\text{RF}} t} \hat{F}_+ - e^{-i\omega_{\text{RF}} t} \hat{F}_- \right) \\
&\approx \mp \frac{1}{2} \frac{k_{3y}}{\|\mathbf{k}_3\|} |\Omega_{23}| \left(\cos[\mathbf{k}_{32} \cdot \mathbf{x} - (\omega_{32} \mp \omega_{\text{RF}})t + \phi_{23}] \hat{F}_x \right. \\
&\quad \left. - \sin[\mathbf{k}_{32} \cdot \mathbf{x} - (\omega_{32} \mp \omega_{\text{RF}})t + \phi_{23}] \hat{F}_y \right). \\
\end{aligned} \tag{C.16}$$

The complete Hamiltonian in the rotating frame after doing the rotating wave ap-

proximation is then

$$\begin{aligned}
\hat{H} = & \frac{1}{2} \frac{|\Omega_{12}|}{\|\mathbf{k}_1\|} \left(\left(k_{1x} \sin[\mathbf{k}_{21} \cdot \mathbf{x} - (\omega_{21} \mp \omega_{\text{RF}})t + \phi_{12}] \pm k_{1y} \cos[\mathbf{k}_{21} \cdot \mathbf{x} - (\omega_{21} \pm \omega_{\text{RF}})t + \phi_{12}] \right) \hat{F}_x \right. \\
& \left. + \left(\pm k_{1x} \cos[\mathbf{k}_{21} \cdot \mathbf{x} - (\omega_{21} \mp \omega_{\text{RF}})t + \phi_{12}] \mp k_{1y} \sin[\mathbf{k}_{21} \cdot \mathbf{x} - (\omega_{21} \pm \omega_{\text{RF}})t + \phi_{12}] \right) \hat{F}_y \right), \\
& \frac{1}{2} \frac{|\Omega_{23}|}{\|\mathbf{k}_3\|} \left(\left(k_{3x} \sin[\mathbf{k}_{32} \cdot \mathbf{x} - (\omega_{32} \mp \omega_{\text{RF}})t + \phi_{23}] \pm k_{3y} \cos[\mathbf{k}_{32} \cdot \mathbf{x} - (\omega_{32} \pm \omega_{\text{RF}})t + \phi_{23}] \right) \hat{F}_x \right. \\
& \left. + \left(\pm k_{3x} \cos[\mathbf{k}_{32} \cdot \mathbf{x} - (\omega_{32} \mp \omega_{\text{RF}})t + \phi_{23}] \mp k_{3y} \sin[\mathbf{k}_{32} \cdot \mathbf{x} - (\omega_{32} \pm \omega_{\text{RF}})t + \phi_{23}] \right) \hat{F}_y \right), \\
& + |\Omega_{13}| \sin(\mathbf{k}_{31} \cdot \mathbf{x} - \omega_{31}t + \phi_{13}) \hat{F}_z
\end{aligned} \tag{C.17}$$

In order to go from this rather complicated looking Hamiltonian to the effective time independent Hamiltonian used in Chapter 8 we need to take two steps: first the off resonant coupling terms need to be neglected. This can be more or less safely done since they will be detuned by something on the order of tens to hundreds of kHz. Second we need to go into a second transformed frame using the unitary transformation

$$\hat{U} = \sum_{i \in \{xyz\}} e^{i(\mathbf{k}_i \cdot \mathbf{x} - \omega_i t)} \tag{C.18}$$

and eliminate the terms that are proportional to $\exp(i\omega_{ij}t)$. The neglected terms of the Hamiltonian in Equation C.17 have the effect of slightly shifting the eigenenergies of the effective Hamiltonian from Equation 8.8. We interpret this shifts in energy as coming from new effective Raman coupling strengths that slightly differ from our calibrations performed by measuring the Rabi frequencies of individual pairs of

Raman beams.